ARTICLE

Luminescent Silver Nanoclusters Decorated on ZnO Tetrapods: Detailed Understanding of Their Role on Photoluminescence Features

Virtual EventReceived 00th January 20xx,
Accepted 00th January 20xx

DOI: 10.1039/x0xx00000x

Joana Rodrigues[†a*], Charline Becker[†b], Nabiha Ben Sedrine[a], Marius Kamp[c], Lorenz Kienle[c], Rainer Adelung[d], Yogendra Kumar Mishra[e], Wolfgang J. Parak[b], Indranath Chakraborty[b*], Maria Rosário Correia[a], Teresa Monteiro[a*]

Optical spectroscopic measurements are conducted on luminescent silver nanocluster (AgNCs) decorated ZnO tetrapods (ZnO Tp), AgNC@ZnO Tp, synthesized via a colloidal route. Their properties are compared with the corresponding AgNCs and ZnO Tp to understand their impact on photoluminescence (PL). Raman spectroscopy reveals high structural integrity of the ZnO structure in the AgNC@ZnO Tp. PL analysis of the ZnO Tp shows a well-resolved near band edge emission and a green band comprised of overlap of at least three emitting optical centres. The addition of AgNCs to ZnO Tp in the hybrid material enhances the emission from ZnO surface states. In the case of the recombination of the AgNCs in water solution, it is dominated by a red emission band peaked at ~1.9 eV. The PL excitation spectra monitored at the band maximum reveal that the red PL of AgNCs is preferentially populated by well-defined excitation bands corresponding to discrete electronic transitions. A shift to lower energies of the AgNCs' emission occurs in the AgNC@ZnO Tp hybrids when excited with energies below the ZnO bandgap. A gradual loss in PL intensity of the AgNCs is observed in the hybrids with increasing time, which is consistent with their coalescence to transform on larger Ag nanoparticles (NPs) on the tetrapod surface, as revealed in confocal microscopy.

1 Introduction

Ultra-small atomically precise metal nanoclusters (NCs) are emerging materials with unique optical and photo-physical properties [1,2]. They are composed of few atoms (namely Au, Ag, Cu, etc.) and protected by some ligands (thiols, phosphine, selenols, etc.) with the chemical formula $M_x(L)_y^Z$, where *x*, *y*, and *z* are the number of metal (M) atoms, the number of ligands (L) and overall charge of the system (z), respectively [1]. A great variety of such NCs comprised of different M and L have been synthesized and characterized, among which Au has been primarily studied owing to its high stability [3]. Yet, reports on AgNCs [4–7] have also been attracting attention in the scientific community, and many new AgNCs with precise crystal structures are established nowadays (for example, $Ag_{25}(SR)_{18}$ [8], $Ag_{29}(S_2R)_{12}$ [9], $Ag_{44}(SR)_{30}$ [10,11], etc., where SR stands for thiolates).

Indeed, these metal NCs exhibit extraordinary features that hold enormous potential to modify the properties of other material systems in the desired manner, strongly depending on how they have been integrated into other materials. For instance, when combined with other nanostructures, noble metal NCs often show distinctive properties. Som *et al.* [12] reported that the incorporation of $Ag_{44}(MBA)_{30}$ NCs (MBA: 4-mercaptobenzoic acid) on Te nanowires (NWs) creates a unique bilayer assembly of the resultant hybrid material at the liquid-air interface, which is induced by the inter nanocluster hydrogen bonding through the MBA ligands. However, glutathione (GSH) protected $Ag_{32}(SG)_{19}$ reacts with the Te NWs' surface to form silver islands at different positions on the NWs that, upon annealing, are transformed to dumbbell-shaped silver-tipped Te NWs [13]. Ghosh *et al.* [14] have reported the coalescence of atomically precise NCs on the graphene surface, which transforms smaller NCs to bigger NCs. From all these reports, it is quite clear that these metal NCs react differently with different material surfaces, which are determined mostly by the physicochemical properties of both the NCs' and foreign materials' surfaces.

In general, under wet chemical conditions, these ultra-small metal NCs exhibit a strong tendency towards agglomeration, which is often undesired [15,16]. Therefore, to access their unique properties, suitable material backbones would be needed, having the capability to localize them on the surface. It gets more interesting when the underneath backbones also exhibit attractive properties desirable for many applications. Such a system may be very advantageous in

[a.] *Department of Physics & I3N, University of Aveiro, 3810-193 Aveiro, Portugal*
[b.] *Department of Physics and Center for Hybrid Nanostructure (CHyN), Universität Hamburg, Luruper Chaussee 149, Hamburg 22761, Hamburg, Germany*
[c.] *Institute for Materials Science, Synthesis and Real Structure, Kiel University, Kaiserstraße 2, 24143 Kiel, Germany.*
[d.] *Institute for Materials Science, Functional Nanomaterials, Kiel University, Kaiserstr. 2, D-24143, Kiel, Germany*
[e.] *Mads Clausen Institute, NanoSYD, University of Southern Denmark, Alsion 2, 6400, Sønderborg, Denmark*
† These authors contributed equally
* Email corresponding authors: joana.catarina@ua.pt (JR); indranath.chakraborty@physik.uni-hamburg.de (IC); tita@ua.pt (TM)
Electronic Supplementary Information (ESI) available: See DOI: 10.1039/x0xx00000x

several senses. These very active NCs sitting on the surface introduce many exciting features in the underneath backbone, resulting in an advanced hybrid system [17–20]. In this way, the properties of these NCs and the underneath backbone are simultaneously accessible for the desired application.

Zinc oxide (ZnO) is a semiconductor that has been thoroughly studied by the scientific community for several decades, and its interest remains intensely active. This is not just only due to being environmentally friendly, low production cost, easiness of synthesis, enabling simple control of the size, morphology and, subsequently, the surface area of its nanostructures, but also in virtue of properties like its wide bandgap energy (~3.4 eV at low temperature), physical and chemical stability, intense PL signal, among others [21–26]. Therefore, countless reports can be found in the literature concerning the production, characterization, and application of this semiconductor, especially when produced at the nanoscale [19,25,27–32]. More recently, the formation of hybrids between ZnO and other materials, namely metal nanoparticles (NPs) [33–35], metal oxides [20,36–39] or carbon-based materials [17,18,40–42], have been continually attracting attention, since the synergetic combination of the different materials is expected to give rise to enhanced and even tailored properties [20,37]. For instance, previous PL studies conducted on ZnO tetrapodal structures produced by flame transport synthesis (FTS) and mixed with different metal oxide compounds (M_xO_y and $Zn_xM_{1-x}O_y$ with M = Fe, Cu, Al, Sn, Bi) [20,37] showed that the PL outcome was strongly dependent on the compound used to form the hybrid network. Moreover, it was demonstrated that their gas sensing properties, particularly selectivity, could also be tuned as a function of the type of M element and its content ratio on the ZnO-based networks, evidencing an enhanced performance when compared with the ones containing only ZnO tetrapods (ZnO Tp) [20,37]. Similar tetrapodal networks were also used to form hybrids with C_{60} molecules [17], resulting in changes in the PL outcome of the hybrids depending on the amount of C_{60} covering the ZnO_Tp, namely in the near band edge (NBE) region. The relative intensity of the transitions in this spectral range increases (when compared to the visible spectral region) with the amount of C_{60} at the surface of ZnO Tp, with particular emphasis on the 3.31 eV emission, which has been assigned to the presence of surface defects in the ZnO structures [17]. A similar trend was also found in microrod samples produced by the same technique (FTS) [18]. Moreover, an enhancement in the relative intensity of the free exciton (FX) recombination was also identified, suggesting that an increase of the free carrier concentration is favoured rather than being captured through the shallow donors under the used conditions. Besides, PL excitation (PLE) measurements revealed that a steeper absorption and a slight shift towards the expected bandgap of pure ZnO was recorded with increasing C_{60} amount, up to a certain threshold where agglomeration of the C_{60} molecules was seen to occur. This reduction in the band tail states is an indication that the population of those electronic states is being reduced, pointing to charge transfer from ZnO to C_{60}. Charge transfer in the opposite direction (C_{60} to ZnO) was also corroborated either by the increase in the NBE intensity and the appearance of other visible (~2.77 eV, 448 nm) and near-infrared absorption bands in the samples with C_{60} on the surface. Indeed, by exciting the hybrid samples with such energy, the ZnO Tp's green luminescence (GL) could be identified.

Atomically precise NCs present several similarities to molecules like C_{60}, namely the discreteness of the energy levels. In this work, tetrapod shaped ZnO structures have been selected as appropriate three-dimensional (3D) backbone to integrate luminescent AgNCs on their surface, and the structure-property relationship of the hybrid 3D nanosystems is investigated in detail. We report a thorough spectroscopic analysis on the produced samples by using room temperature (RT) Raman spectroscopy, optical extinction, PLE, excitation-energy and excitation-density dependent PL, time-resolved PL (TRPL), and temperature-dependent PL to investigate the changes in the optical features of both components when placed together.

2 Experimental Details

2.1 $Ag_{29}(DHLA)_{12}$ NCs synthesis

DHLA protected Ag_{29} NCs were prepared according to Van der Linden *et al.* [43,44]. In brief, lipoic acid (LA) was dissolved in water in the presence of $NaBH_4$. Then silver precursor, $AgNO_3$, was added, followed by $NaBH_4$, and the mixture was kept stirring for 4.5 h at RT. The details of the NCs synthesis and characterization can be found in the Electronic Supplementary Information (ESI) file.

2.2 ZnO tetrapod synthesis

ZnO Tp were synthesized via FTS, as described by Smazna *et al.* [17]. In brief, Zn metal particles (average diameter around 5 µm) in powder form were mixed with polyvinyl butyral powder (PVB) in the weight ratio of 1:2 as the primary precursor material. The precursor mixture was filled in a ceramic crucible and then mounted in a muffle furnace heated to 900 °C for 30 minutes. The transformation of Zn metallic particles into ZnO tetrapods directly occurred in the flame inside the furnace via the solid-vapour-solid process (details are mentioned in the ESI). A detailed description of the FTS process and its modified variant has been reported in previous works [17,18,45,46]. After the growth process, the furnace is left for natural cooling and a white snow-like powder, which is tetrapod shaped ZnO micro- and nanostructures, is carefully harvested from and accordingly used as backbones for decoration of ultrasmall Ag nanoclusters.

2.3 Synthesis of AgNC@ZnO Tp

The AgNCs were integrated with the ZnO Tp via a solution-based incubation approach. First, 4 mL of the as-synthesized AgNCs solution was concentrated through centrifuge 3 kDa filtration (final concentration of Ag in the NCs is C_{Ag}=0.159 mg mL^{-1} measured by inductively coupled plasma mass spectrometry). Then, ZnO Tp (5 mg) were incubated in 0.5 mL of concentrated AgNCs solution for 5 h under constant shaking. After this time, unreacted AgNCs were removed from the ZnO Tp surface through centrifugation (1000 rpm, 1 min). The precipitate was collected, rewashed with deionized water, dried at RT, and stored for further experiments.

2.4 Materials' characterization

The produced materials were morphologically, structurally, and optically characterized by transmission electron microscopy (TEM), scanning transmission electron microscopy (STEM),

Raman spectroscopy, optical extinction, RT PLE, excitation-energy and excitation-density dependent PL, TRPL, and temperature-dependent PL. Details on the used techniques are fully described in the supporting information.

3 Results and Discussion

A scheme of the dihydrolipoic acid (DHLA) protected Ag_{29} NCs decorated ZnO Tp (AgNC@ZnO Tp) synthesis is represented in Figure 1A, and corresponding photographs are shown in the insets. The ZnO Tp have a white colour appearance under visible light and evidence ultraviolet and green emissions using UV excitation at RT, respectively (Figure 1A, inset). At the same time, AgNCs in water solution show an intense red emission under the same excitation conditions (Figure 1A, inset). Upon visible light observation, the white colour of the dispersion containing the ZnO Tp transforms to orange due to AgNCs incorporation into the hybrid material, i.e. the formation of AgNC@ZnO Tp, which also shows a faint yellow-orange luminescence under UV excitation (Figure 1A, inset).

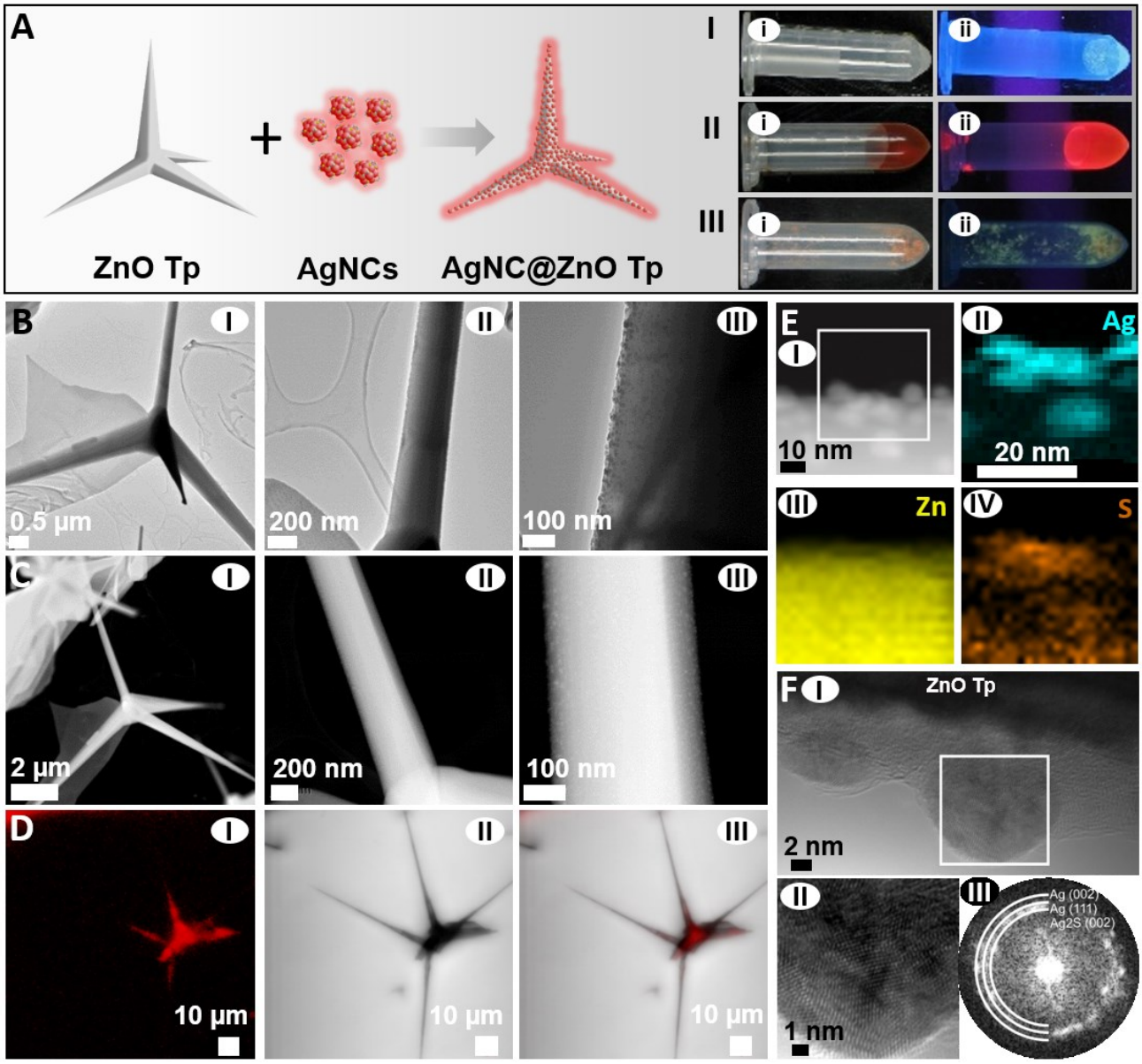

Figure 1 - (A) Scheme of the AgNC@ZnO Tp synthesis. The insets show the ZnO Tp (in water) (I), AgNCs (synthesis solution) (II), and AgNC@ZnO Tp hybrid (dry) (III) under visible light (i) and UV light excitation (ii). (B) TEM and (C) High-angle annular dark-field (HAADF)-STEM images of the AgNC@ZnO Tp hybrid at different magnifications (I-III). (D) Confocal laser scanning microscopy (CLSM) images of the AgNC@ZnO Tp excited at 3.06 eV/405 nm; (I) showing the PL below/above 2.0 eV/615 nm, (II) bright-field image, and (III) the overlay of bright-field and PL intensity image. (E) HAADF-STEM image (I) with EDX elemental mapping for the elements Zn (II), Ag (III), and S (IV). (F) HRTEM micrograph (I), a magnified HRTEM micrograph of an AgNC (II), and the respective FFT (III) are shown.

The morphology of these materials was investigated by TEM and STEM, as shown in Figures 1B and 1C. The highly magnified images (cf. 1B (III) and 1C (III)) of the AgNC@ZnO Tp surface show the presence of NPs with larger diameters than expected for the AgNCs. These investigations indicate the agglomeration of AgNCs in the high-energy electron beam that might be supported by the decomposition of DHLA linker molecules. Consequently, TEM investigations represent decomposed AgNCs, however, a homogeneous distribution of decomposed AgNCs on the ZnO Tp surface is verified (Figures 1B and 1C). Furthermore, STEM-Energy Dispersive X-ray spectroscopy (EDX) elemental mapping confirms the presence of zinc (Zn), silver (Ag), and sulfur (S), whereby the S signal might predominantly arise from the decomposed linker molecules (DHLA) located at Ag and ZnO surfaces (Figure 1E). A high-resolution TEM (HRTEM) micrograph depicted in Figure 1F, shows crystalline decomposed AgNCs. Investigation of the fast Fourier transformation (FFT) (Figure 1F(III)) shows intensities on concentric rings from metallic Ag (*F*m-3m space group and lattice parameter a=4.09 Å), however, additional reflection intensities of Ag_2S (*I*m-3m space group and lattice parameter a=4.89 Å) indicate the partial formation of Ag_2S phase in the electron beam caused by *in situ* reactions of Ag with S from decomposed linker molecules. Since AgNCs are photoluminescent in nature (this will be further discussed in the following section), the spatial distribution of the emitting AgNCs on the ZnO Tp surface can be observed using confocal laser scanning microscopy (CLSM) as represented in Figure 1D.

Raman spectroscopy measurements were carried out to evaluate the change in ZnO Tp lattice vibrational modes due to the hybrid formation. Figure 2 (see also Figure S1 in ESI) depicts the Raman spectra of ZnO Tp and AgNC@ZnO Tp acquired in different points of the samples obtained with 2.8 eV/442 nm excitation, which is resonant with the AgNCs' absorption energy, as shown in Figure S3. Both cases evidence the typical lattice vibrational modes of the ZnO hexagonal wurtzite structure that are active in Raman: A_1, E_1, and E_2, as well as its overtones and combined modes related with second-order Raman scattering processes, as reported by Cuscó *et al.* [47]. The more intense second-order features occur in the high frequency (1000 cm^{-1} - 1200 cm^{-1}) and involve longitudinal optical (LO) phonon modes. The presence of second-order and/or first-order symmetry forbidden Raman features [48,49] are due to the relaxation $\vec{k} = \vec{0}$ moment first-order selection rules, meaning that infinite correlation length is lost and the phonon eigenstates are no longer described by plane waves. To the breakdown of the translation symmetry lattice, beyond the occurrence of defects or impurities, the size of the ZnO Tp crystallites can contribute as well [50]. The differences observed in the relative intensity of the ZnO Tp related vibrational modes for the same sample may arise from polarization effects caused by the different orientations between the ZnO Tp and the incidence wavevector of the laser beam [47,51–53].

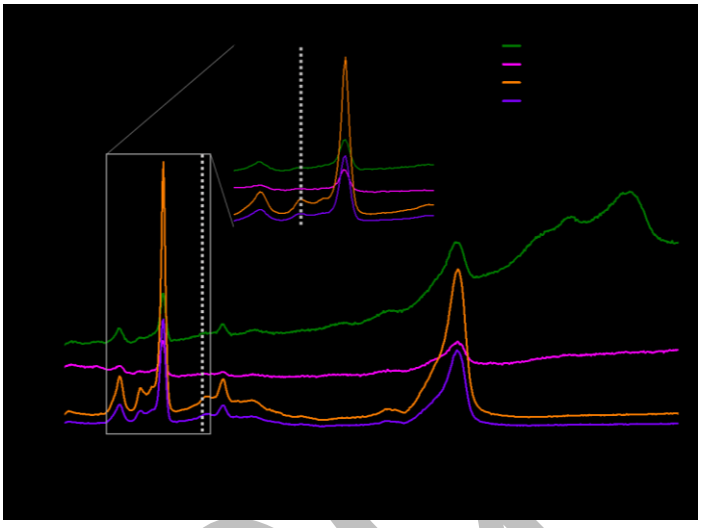

Figure 2 - RT Raman spectra obtained with 2.8 eV/442 nm laser excitation (using a 0.3 neutral density filter (ND0.3)) for both ZnO Tp and AgNC@ZnO Tp hybrids, probing different points of the samples. Vibrational modes indexation is according to reference [47]. The spectra were shifted vertically for clarity. Inset: enlarged view of the E_2^{high} mode spectral region.

In the case of the AgNC@ZnO Tp hybrid, besides the polarization effects, also the high absorption of the incident and scattered light by the AgNCs (Figure S2) contributes to the reduction in the relative intensity of the ZnO Tp Raman bands. Indeed, in this case, the E_2^{high}/LO overtone ratio was found to be lower than the one identified in the ZnO Tp (~1 vs 1.5). Nevertheless, it is worth noting that for the same sample, this ratio is similar for the distinct spots probed. The increase in the relative intensity of the LO overtone in the AgNC@ZnO Tp hybrid is likely to be related to the different resonance profiles in the two samples upon 442 nm (~2.8 eV) photon excitation owning to the presence of the AgNCs, affecting the outgoing resonance process, translated into an increase of the LO overtone contribution. Besides,, additional broad Raman bands appear in the 1400–1700 cm^{-1} region, which should be associated also with those ligands [54,55]. Excitation density-dependent studies were also conducted for ZnO Tp and AgNC@ZnO Tp hybrids (Figure S1) and no change in the frequency or broadening of the Raman signal was observed by increasing the excitation density, suggesting that the diffusion of local heating is very efficient. Furthermore, the overall shape of the Raman spectrum is maintained, indicating high stability of the surface.

PL spectroscopy is an important tool for characterizing AgNC@ZnO Tp hybrids considering their visible PL nature. Particularly, it constitutes an excellent mean to assess the presence of both surface and bulk emitting ZnO defects, charge transfer processes and other physical interactions that may occur in the hybrids [25,56]. As mentioned, the size distribution of the here studied AgNCs in water solution gives rise to an extinction spectrum involving molecular-like discrete energy levels, as shown in Figure S2. Well-resolved absorption bands with maxima at 3.70 eV/335 nm, 2.85 eV/435 nm, and 2.48 eV/500 nm occur, in line with previously reported works [43,57]. As such, exciting the samples close to these energies should lead, upon relaxation, to the AgNCs' PL. This is

displayed in Figure 3, where the normalized RT PL/PLE spectra are presented for AgNCs (in water solution), ZnO Tp, and AgNC@ZnO Tp. For the case of the AgNCs in water solution (Figure 3A), an intense red emission peaked at 1.9 eV/652 nm and with a full width at half maximum (FWHM) of 250 meV is identified when the samples are excited with a wide range of high energy photons, in accordance with the results presented in Figure 1. As shown by the PLE spectra monitored at the emission band maximum, and in agreement with the measured optical extinction (Figure S2), the excitation bands responsible for the population of the emitting states spread over the region ~2.0 - 3.7 eV/620 - 335 nm. Three main excitation maxima located at ~2.48 eV/500 nm, ~2.79 eV/446 nm, and ~3.07 eV/403 nm can be distinguished. The spectral shape of the measured PL and PLE spectra of the AgNCs in water solution are similar to the ones reported in the literature [43,57–60]. Additionally, it should be emphasized that the PLE and optical extinction spectra evidence the same spectral features, meaning that the observed red PL from the AgNCs in water solution is indeed preferentially populated through discrete-like excited levels of the silver nanoclusters. Figure 3B shows the RT PL and PLE spectra of the ZnO Tp, while Figure 3C displays the spectra of the AgNC@ZnO Tp hybrids. Upon above bandgap excitation, the ZnO Tp exhibit a commonly reported PL [17,22,23,25,61] characterized by shallow levels recombination corresponding to the UV NBE emission band and, at lower energies, a deep level recombination dominated by a broad GL. At this temperature, the relative intensity of the GL is higher than the NBE. The PLE monitored at the GL band maximum (~2.43 eV/510 nm) indicates that the ZnO Tp luminescence is mainly populated by photons with energy equal to or higher than the ZnO bandgap. For the case of the AgNC@ZnO Tp hybrid (Figure 3 C), the combination of the two materials results in noticed changes in the measured PL. On the one hand, the spectral shape of the ZnO emission is unchanged under UV excitation and the PLE spectra taken at the GL of the hybrid evidence the same steeper ZnO bandgap absorption, indicating that the ZnO emission is populated by photons with energy equal or higher than the semiconductor bandgap. On the other hand, by exciting the samples with such high-energy photons, we were unable to observe the red light from the AgNCs, as previously detected in water solution. Indeed, for the AgNC@ZnO Tp hybrid, the emission of the AgNCs shifts to lower energies and the PLE monitored on the emission band maximum evidences significant changes when compared with the one in water solution. Particularly, a FWHM increase of the discrete and size-tunable electronic excitation bands is detected, which is accompanied by a decrease of the bands' relative intensity and by the absence of the high-energy electronic excitations. Consequently, the red/near-infrared PL from the AgNCs on the hybrid is only observed by using low-energy photons as the excitation source, namely the ones with energy in the blue/green region at ~2.8 eV/442 nm and ~2.44 eV/508 nm, matching the AgNCs' absorption/excitation bands, as shown in Figure 3C. This is likely related to the interaction between the AgNCs and the ZnO Tp, promoting charge transfer processes between their electronic levels/bands. A more detailed discussion on the subject is presented below including the PL data collected at low temperature.

By comparing the PL spectra measured under the same lower excitation density (using a Xe lamp) and energy (~2.8 eV/442 nm) conditions for AgNCs in water solution and AgNC@ZnO Tp hybrids, the maximum of the red band shifts from ~1.9 eV/652 nm to ~1.73 eV/717 nm, respectively (Figures 3A and 3B).

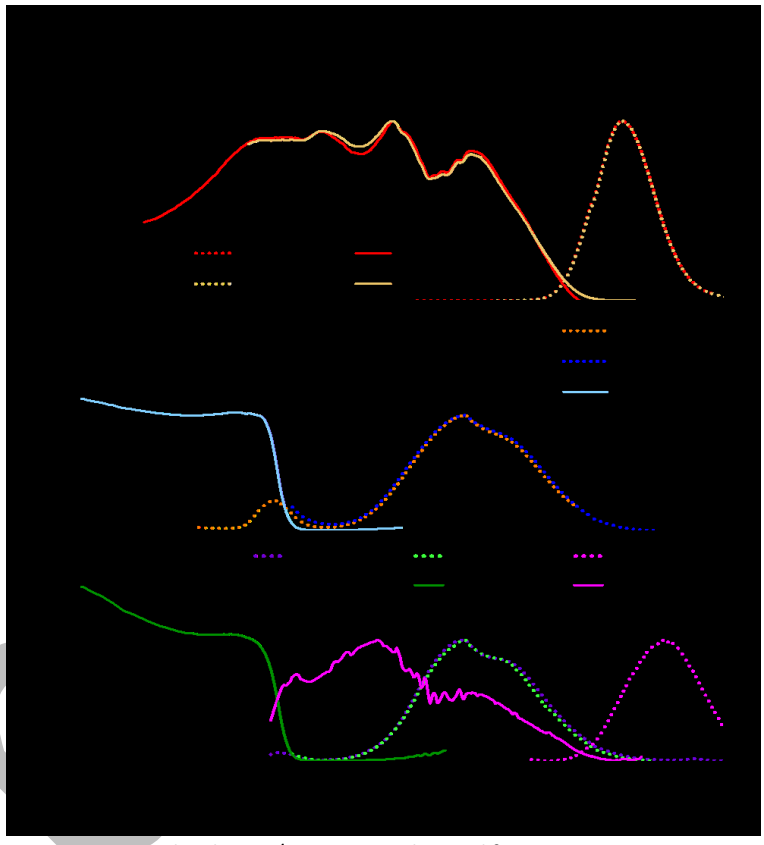

Figure 3 - Normalized RT PL/PLE spectra obtained for AgNCs in water solution (A), ZnO Tp (B), and AgNC@ZnO Tp hybrid (C). The asterisk denotes an artefact of the system. Solid lines correspond to PLE spectra, while dashed lines denote PL spectra.

In the latter case, the FWHM of the clusters' PL corresponds to 360 meV, which is higher than the 250 meV measured for the emission of the AgNCs in water solution [59,62]. Such behaviour may originate from the AgNCs' particle-particle interplay with the environment, whose dielectric properties resulted in changes in the energy separation of the electronic levels [59,62,63].

Additional excitation-density dependent PL was performed for ZnO Tp and AgNC@ZnO Tp, as shown in Figure 4 (see also Figure S3), by applying neutral density filters to the 3.81 eV/325 nm He-Cd laser line. For the case of the ZnO recombination, it is well established that broad emission bands can be due to the spectral overlapping of several emitting defects [22,25,64,65]. This is the case of the here studied GL observed either in the ZnO Tp or in the AgNC@ZnO Tp hybrids, showing a similar spectral shape and FWHM in both cases. The excitation-density dependent PL studies evidence that the GL shifts to lower energies with increasing excitation density, with a more pronounced effect on the hybrid (Figure S3A). Indeed, while in the case of the ZnO Tp sample (Figure 4A), barely any shift of the peak position was observed within the excitation density range used, for the AgNC@ZnO Tp hybrids (Figure 4B) the peak position of the GL was seen to shift. This shift can be justified by the presence of several recombination channels, whose relative intensity depends on the

excitation density. Indeed, when excited by the laser, the GL of the AgNC@ZnO Tp hybrids shows a noticed asymmetry, evidencing more than one recombination channel contributing to the overall observed emission. By reducing the laser excitation density to 1% of the nominal one (Figure S3B), one can plainly see that the spectral shape of the emission bands of the ZnO Tp and AgNC@ZnO Tp samples became coincident. Nevertheless, even excited with only 1% of the nominal laser power, the peak position of the GL still appears at lower energy than the one recorded when excited with the Xe lamp (~2.36 eV/525 nm *vs* ~2.46 eV/504 nm), as a reduced power excitation is provided by the lamp. Therefore, we can conclude that under low excitation density the high-energy components of the GL dominate, while increasing the excitation density favours the recombination of the lower energy component.

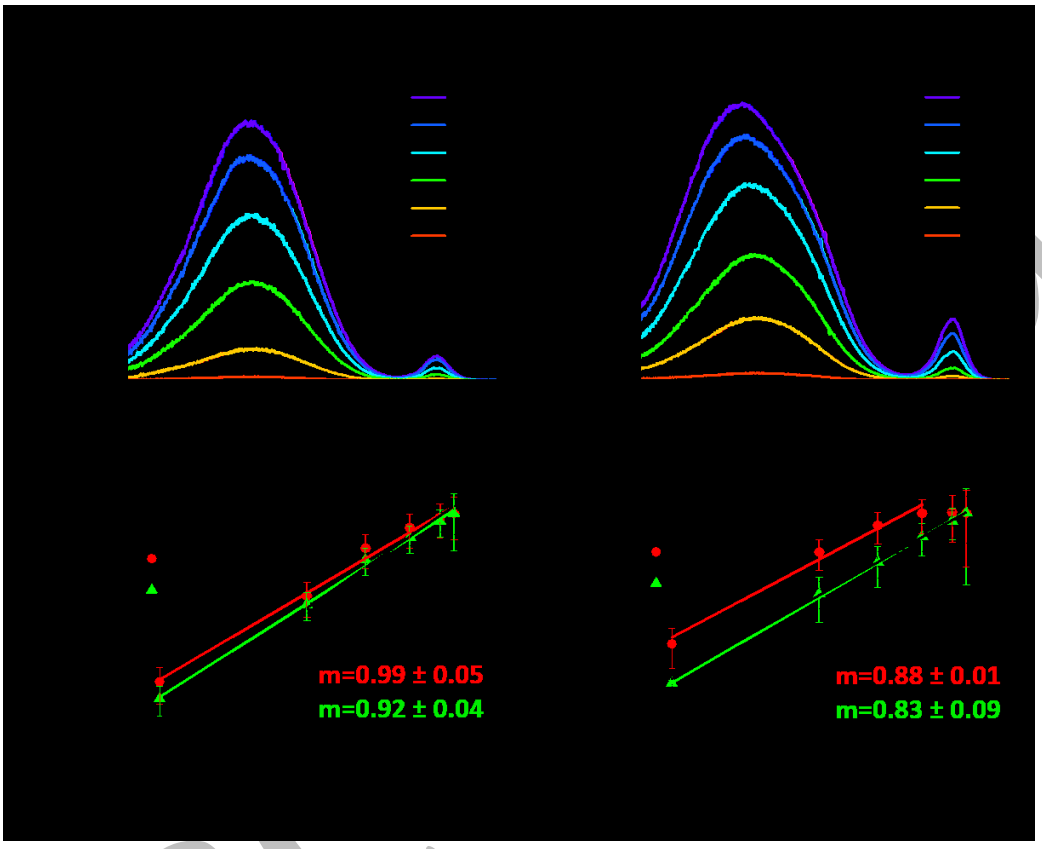

Figure 4 - Density excitation-dependent PL spectra acquired at RT for ZnO Tp (A) and the AgNC@ZnO Tp hybrids (B) under 3.81 eV/325 nm excitation. Graphical representation of the increase of the normalized intensity as a function of the excitation density for PL bands peaked at ~2.6 eV, ~2.4 eV and ~2.2 eV for ZnO Tp (C) and AgNC@ZnO Tp hybrids (D).

As the peak positions and spectral shape found for the GL in both samples are different at high excitation density and become coincident for low excitation density (Figure S3B), it was assumed that the same recombination channels are present in both samples. Therefore, the spectra were deconvoluted into Gaussian components, allowing to gain more insight regarding the optical centres present in the here reported samples. As such, an adequate fit was obtained considering three components contributing to the overall visible GL. Indeed, Figure S4A and B evidence the presence of these components, peaked at~2.6 eV/477 nm, ~2.4 eV/517 nm, and ~2.2 eV/564 nm in both ZnO Tp and AgNC@ZnO Tp hybrids, however with different relative intensities, resulting in the observed shift of the peak position for the GL in the two samples. Moreover, Figure S4C and D reveals that under 1% of the initial excitation intensity (I_0) the component peaked at ~2.4 eV/517 nm becomes the dominant one in both samples, thus resulting in a similar spectral shape and peak position, as observed under excitation with the Xe lamp.

Regarding the integrated PL intensity of the GL components as a function of the excitation density of the here studied samples, the data can be fitted to a power law, $I \propto P^m$, where I is the luminescence intensity, P is the excitation power and m is a parameter that represents the slope in a log-log representation of I and P [66]. This relationship gives information regarding the type of transition involved. When $m < 1$, and according to the rate equations, it is proposed that the nature of the radiative transitions involves donor-acceptor pairs (DAPs) or free-to-bound carrier recombination, while when $1 < m < 2$ an exciton-like transition should be involved [66]. All the components exhibit a slope close to 1 (Figure 4C and 4D), meaning that a DAP, free-to-bound or excitonic-like nature for the observed recombination channels should be considered. However, the fact that no shift in the peak position was observed by reducing the excitation density points to a free-to-bound recombination or excitonic-like type [67,68].

RT time-resolved PL (TRPL) studies (Figure S5) revealed that once again no shift in the peak position was identified with increasing delay times. The TRPL measurements were conducted under 325 nm (~3.81 eV) excitation for increasing time delays up to 1 ms and using a time window of 10 ms. For both ZnO Tp and AgNC@ZnO Tp samples, the visible band was seen to nearly disappear after a time delay of ~0.2 ms, indicating a lifetime in the range of tens of µs. Additionally, the spectral shape and the peak position of the observed band do not change significantly with increasing delays in either case. The fact that both samples exhibit PL signals with similar spectral shape and lifetime corroborates the assumption of having similar recombination channels contributing to this GL. As previously mentioned, it should be emphasized that the GL is very common in ZnO, either in bulk, layers, or nanostructures [25,64]. Although other broad emission bands in the blue, yellow, and orange/red spectral region have also been reported [65,69,70], the GL is the most described and debated one. However, there is still some controversy regarding the chemical nature of distinct defect emissions and different hypotheses have been proposed to explain them. It is known that several types of defects are responsible for the emissions in the different spectral ranges, but the association between such defects and the observed blue/green/orange/red luminescence have not been yet conclusively established [25,65]. The defect-related luminescence in the green region is frequently ascribed to intrinsic defects in the ZnO matrix, namely oxygen/zinc vacancies (V_O/V_{Zn}), Zn antisites (Zn_O), interstitial Zn atoms, transitions from Zn interstitials to Zn vacancies, and also to extrinsic impurities, as is the case of Cu [71,72]. However, some reports presented convincing evidence that defects located at the surface may also give rise to luminescence bands in the same spectral region [65], which becomes particularly relevant in structures with a high surface area, as is the present case. Thus, despite having similar peak positions and width, the origin of the observed GL may be rather different from sample to sample [22,64] and a single sample can exhibit an overlapped of several of the mentioned contributions.

To get a deeper insight on the mechanisms involved in the different luminescence processes, the samples were cooled down to 11 K. Figure 5A shows a comparison of the 11 K PL spectra of ZnO Tp and AgNC@ZnO Tp hybrids acquired with above ZnO bandgap laser excitation (3.81 eV/325 nm). In both cases, the NBE emission dominates over the visible band. While for the ZnO Tp sample the NBE intensity is around one order of magnitude higher than the GL one, for the hybrid the intensities of the NBE and deep luminescence are comparable. Additionally, the broad unstructured GL band is centred at ~2.43 eV/510 nm in the case of the ZnO Tp samples and at ~2.39 eV/519 nm for the AgNC@ZnO Tp hybrids, likely related with the above discussed distinct contribution of the defects that originate the different recombination channels spectrally overlapped. It should be emphasized that the observed GL at 11 K corresponds to the so-called unstructured GL[22,64].

For the ZnO Tp and AgNC@ZnO Tp hybrids, a well-resolved NBE composed of different recombination channels was recorded, enabling to identify the presence of free exciton (FX), donor bound excitons (D^0X), as well as the 3.31 eV-line and their LO phonon replicas, with an energy separation of ~70 meV [64,73]. An enlargement of the NBE region can be better seen in Figure 5B.

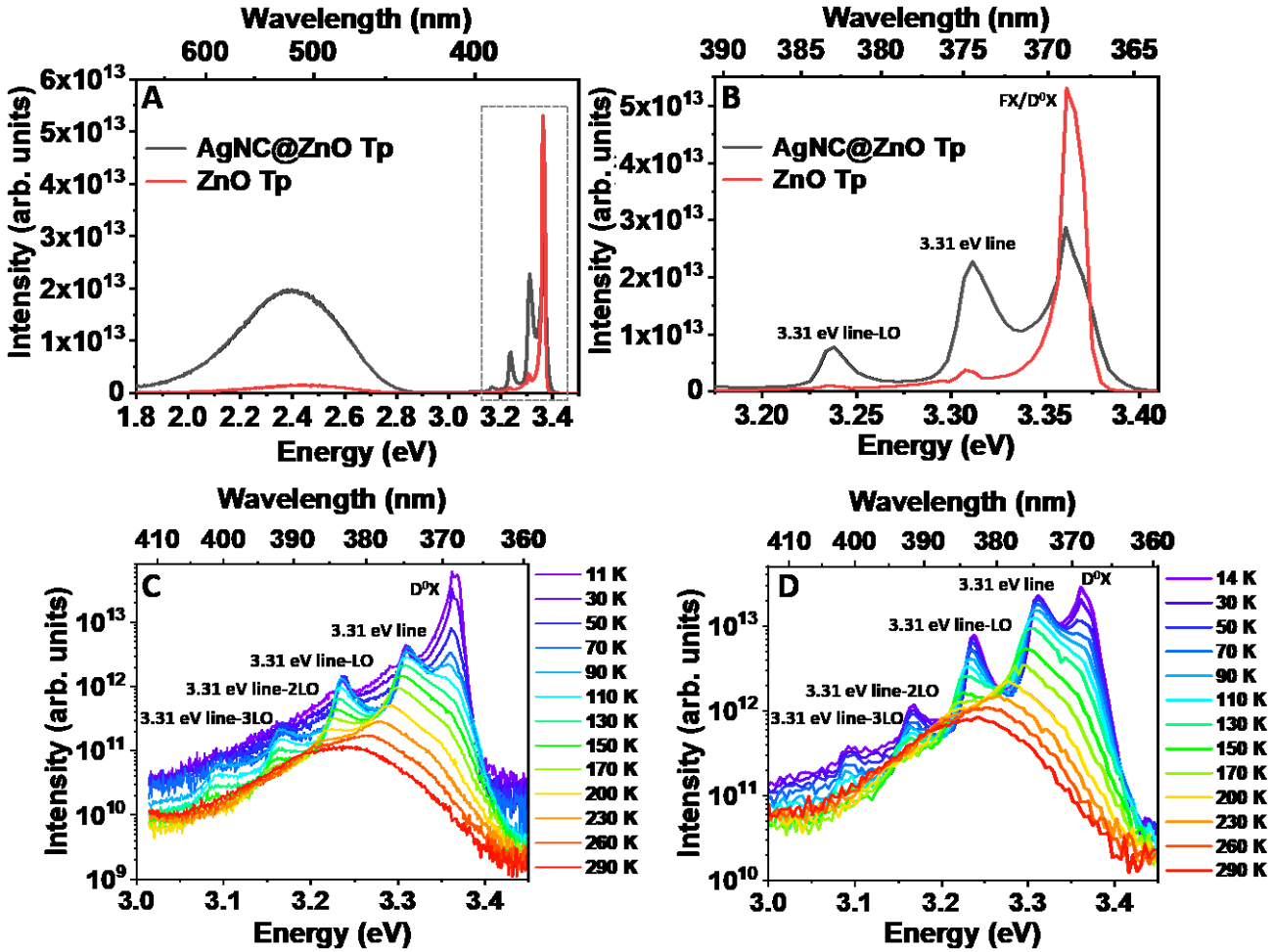

Figure 5 - (A) 11 K PL spectra of ZnO Tp and AgNC@ZnO Tp hybrids under the same alignment conditions. (B) Enlargement of the area marked with a grey dashed line in (A). Temperature-dependent PL study performed with high-resolution steps in the NBE region for ZnO Tp (C) and AgNC@ZnO Tp (D). All spectra were collected with 325 nm (~3.81 eV) excitation.

When a comparison of the NBE recombination for ZnO Tp and AgNC@ZnO Tp hybrids is made, it is straightforward that the relative intensity of the 3.31 eV line regarding the D^0X recombination strongly increased in the hybrid. In the case of the ZnO Tp, the intensity of the FX and D^0X transitions plainly dominate the NBE spectrum, with an intensity of an order of magnitude higher than the one evidenced for the 3.31 eV line. For the hybrid, and similarly to what was observed for the GL *vs* NBE relative intensities, the 3.31 eV has an intensity in the same order of magnitude as the one recorded for the D^0X transition. This 3.31 eV line has been associated with distinct recombination mechanisms. Among them, the most accepted hypotheses for the nature of the centres involved are the presence of surface states and excitons bounded to surface defects [74,75], as well as structural defects-related transitions [76–79]. A work performed by some of the present authors in ZnO microrods grown by laser-assisted flow deposition (LAFD) [23] indicates a strong correlation of this 3.31 eV emission line with the presence of surface states, as identified by the influence of distinct plasma treatments on the recombination line intensity [80]. Thus, even though the chemical nature of the defects that give rise to this transition is unknown, the addition of the AgNCs to ZnO Tp seems to promote a pronounced modification of the metal/semiconductor interface's electric potential. As such, a band bending of the energy bands develops near the material surface together with a depletion region that will influence the ZnO Tp PL by enhancing the population of the existent surface-emitting state(s). Therefore, with the used excitation conditions all the absorbed carriers relax to the ZnO band structure in the hybrid material, improving the surface-related emitting defects, like the ones related to the 3.31 eV emission and the GL, justifying the observed differences in the ZnO Tp and hybrids. A schematic representation of these processes is depicted in Figure 6. Figure 6 (a) displays the proposed energy level diagram for the AgNCs in aqueous solution, based both on the absorbance (Figure S2) and PLE/PL (Figure 3A) data. After the formation of the AgNC@ZnO Tp hybrid, the AgNCs' particle-particle interplay with the environment and with the ZnO Tp surface leads to the changes in the AgNCs electronic levels. PL analysis evidenced that upon 325 nm (~3.81 eV) excitation of the hybrids, only the emission features related to ZnO. Moreover, 14 K PL revealed that the contribution from the surface-related defects (3.31 eV emission line and GL) are enhanced in this case. Therefore, we proposed that when the AgNC@ZnO Tp hybrids are excited with 325 nm (~3.81 eV), charge transfer occurs from the

AgNCs to ZnO, as illustrated in Figure 6b, similarly to what was previously reported for the C_{60} case already discussed in the introduction [17,18]. This means that with energy ~3.81 eV, electrons from the highest occupied molecular orbital (HOMO) of the AgNCs can be excited to the higher energetic states of the lowest unoccupied molecular orbital (LUMO), which energetically placed above the ZnO conduction band (CB) and, afterwards, instead of recombining radiatively inside the NCs, they are transferred for the ZnO Tp energy levels, leading an increase in the population of the ones induced by the surface defects, and subsequently to the intensity of the surface-related radiative recombinations, as is the case the 3.31 eV emission line and some of the defects contributing to the GL. Such phenomenon can also justify the differences in the peak position of the GL observed for the ZnO Tp and AgNC@ZnO Tp hybrids either at RT (Figure 3) and 11 K (Figure 5A) since the preferential population of different defect levels is expected to occur due to the charge transfer when compared to the direct band-to-band excitation of ZnO. The band alignment between the energy levels of the two materials represented in Figure 6b was proposed considering the present electron transfer hypothesis, as these processes can only be efficient if the electronic alignment is favourable. i.e. with the upper LUMO above the CB of ZnO. Hence, when photons with energy in the visible range are employed (*e.g.* 442 nm), the electrons of the AgNCs are excited to the lower LUMO, whose energies are below the one of the ZnO CB, thus do not participate in the charge transfer processes. As so, the radiative recombination between the AgNCs energy levels takes place, leading to the red emission band peaked at ~1.73 eV. The low-temperature PL enables the deconvolution of recombination centres that appear overlapped at RT, which are of particular importance for the identification of the ZnO NBE at higher temperatures. As so, the temperature-dependent PL spectra on the UV-visible spectral range (Figures S6 and S7), as well as high-resolution spectra in the NBE region (Figure 5C and 5D) were collected for the ZnO Tp and the AgNC@ZnO Tp hybrids. As expected, with increasing temperatures, the D^0X dissociates, causing a decrease in the PL intensity due to nonradiative relaxation, accompanied by a redshift due to the bandgap shrinkage. At RT, the NBE is dominated by the FX recombination, typically at ~3.28 eV/378 nm overlapped with the 3.31 eV line (and its replicas) related to the surface-states. A slight shift of the GL peak position towards lower energies is also observed, likely due to the bandgap reduction and/or different relative intensity of the centres that composed this emission.

The PL stability and dynamics of the structural change of AgNCs over time was studied by measuring the PL spectra under 2.8 eV/442 nm excitation and recording time-dependent CLSM images at 3.06 eV/405 nm, as shown in Figure 7. In both cases, the used excitation corresponds to the absorption between discrete levels of AgNCs into the hybrids (see the PLE spectra of Figure 3C). The results show a constant decrease in the PL intensity over 10 days.

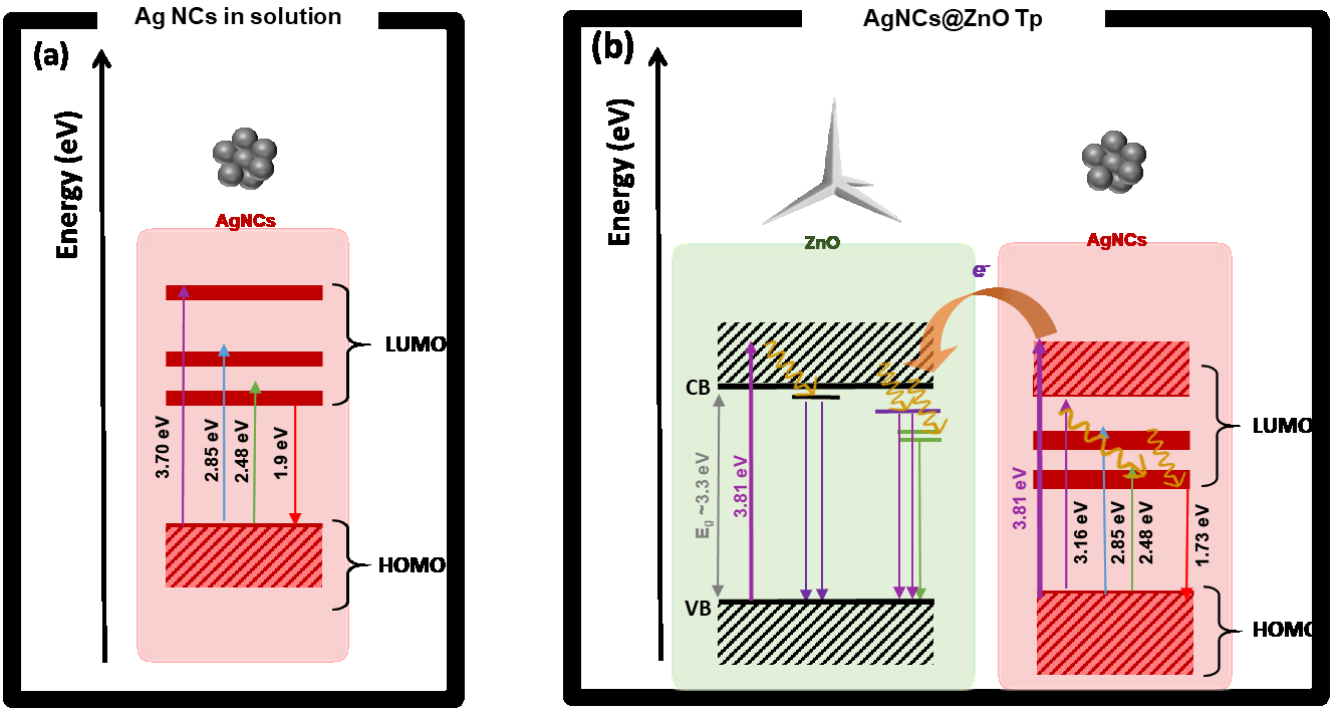

Figure 6 - Schematic representation of the (a) energy level diagram of electronic excitation and emission transitions in the AgNCs and (b)charge transfer processes that may occur between the ZnO Tp and AgNCs upon the hybrid formation. Note that the spacing of the levels is not at scale. CB stands for conduction band, while CV denotes the valence band.

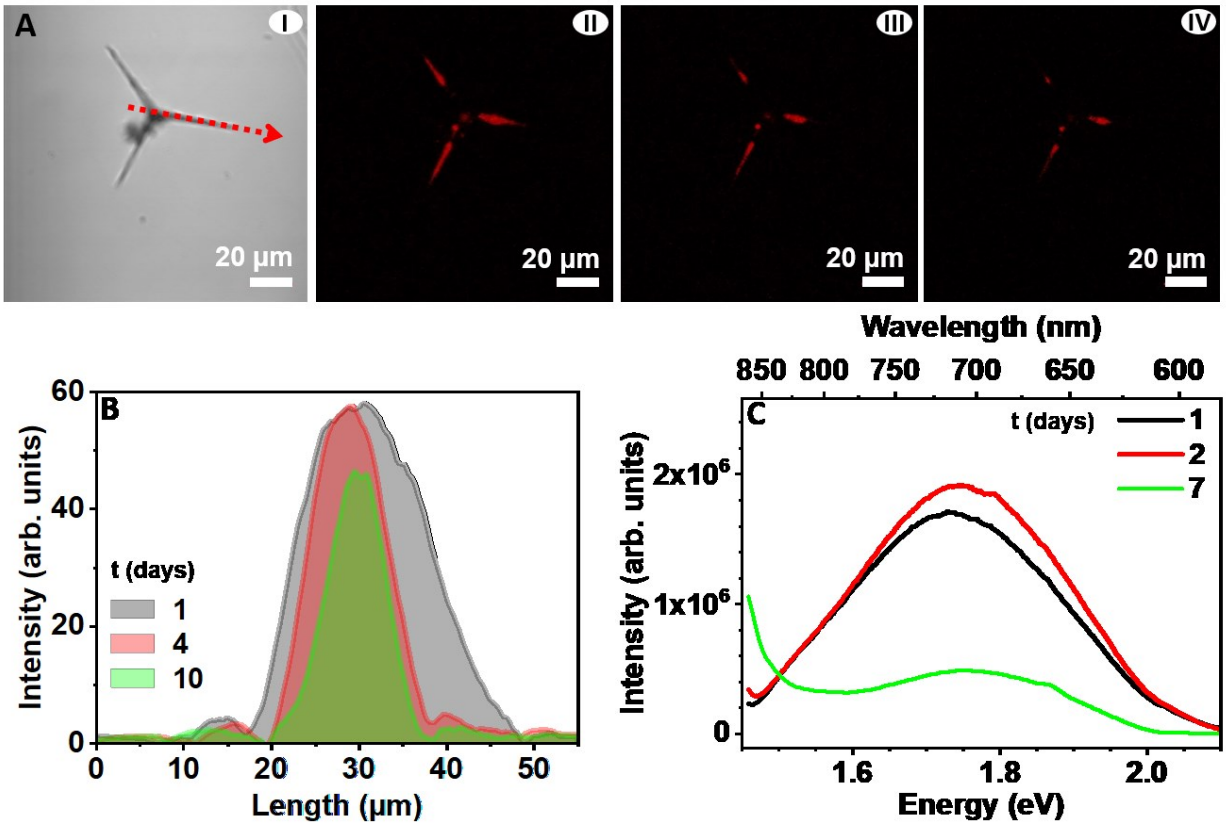

Figure 7 - (A) Intensity change of the AgNCs' PL on a ZnO Tp detected in CLSM ((I) bright-field image) from day 1 (II) to day 4 (III), to day 10 (IV). (B) Graphical representation of the PL intensity change over time. Arrow in (A) shows the axis along which the intensity change was collected. (C) RT PL spectra acquired at 2.8 eV/442 nm excitation for the AgNC@ZnO Tp hybrids after 1, 2 and 7 days of sample's preparation.

The PL intensity profile (Figure 7B) collected along one of the tetrapod arms (Figure 7A red arrow) confirms such change in the NCs' PL over time. Additional support is given by Figure 7C, which displays the PL spectra acquired at different times for the AgNC@ZnO Tp sample. The spectra were acquired under the same measurement conditions and in the same sample (the one used for all the PL studies). As can be seen, the spectral shape is preserved while the overall intensity decreases with increasing time. In fact, after 7 days of sample's preparation, the red PL band exhibits a very low intensity. The decrease of PL intensity in both experiments suggests that the AgNCs' structures changed over time.

ZnO has been used as a platform for several hybrid structures, namely to connect gold nanoparticles (AuNPs) onto their surface via a dithiol linker [81–8]>. This possibility to directly connect thiols to a ZnO surface opens up the possibility of lipoic acid diffusing from the AgNCs to the tetrapod surface.

Conclusions

In summary, AgNCs, ZnO Tp, and AgNC@ZnO Tp samples were analysed in detail by optical spectroscopy techniques. In the first case and by exciting the sample into the higher excited levels of the AgNCs in water solution, a broad red emission band peaked at ~1.9 eV/652 nm was identified. In this case, the photoluminescence excitation spectra monitored at the band maximum reveals that the emission band is preferentially populated by well-defined excitation bands corresponding to discrete electronic transitions with main maxima ~2.48 eV/500 nm, ~2.8 eV/443 nm, ~3.0 eV/413 nm, and ~3.33 eV/372 nm. A similar observation was found in the optical extinction spectrum. For ZnO Tp and AgNC@ZnO Tp samples, and by exciting the samples with photon energy equal or higher than the ZnO bandgap, the typical spectra of ZnO was observed, presenting, at RT, the NBE emission in the UV region and a visible broad band peaked in the green spectral region. The peak position of the green band was seen to be dependent on the excitation density, shifting towards lower energies for higher excitation density, especially in the case of the hybrid. This phenomenon was explained considering the presence of different recombination channels contributing to the overall green emission band, as corroborated by the deconvolution of the band, which revealed the presence of similar optical centres in both samples, but with a distinct response to the excitation density. The presence of the AgNCs in the hybrids promotes a noticed population of the emitting states in the ZnO host, namely the ones related to surface states recombination. This was particularly evident when the samples were excited with the 3.81 eV/325 nm laser line and analysed at low temperature. In that case, the relative intensity of the green luminescence was seen to increase regarding the NBE after hybrid formation, together with an increase of the surface-related 3.31 eV

emission line intensity when compared to the ZnO free and bound exciton recombination.

For the AgNC@ZnO Tp hybrids, the metallic nanoclusters' emission is shifted to lower energies when compared with the emission in an aqueous solution, showing a peak position at ~1.73 eV/717 nm, likely due to the influence of the surrounding medium. In this case, the emission is no longer observed with photon excitation higher than 3.27 eV/379 nm, as identified by the photoluminescence excitation spectra. Indeed, the widening and low-energy shift of the excitation bands indicate noticed changes in the energy location of the discrete levels of metallic clusters when placed on ZnO Tp. Finally, analysing the hybrid sample during different days after its preparation demonstrates its degradation over time, with the red/NIR emission associated with the AgNCs almost vanishing after one week, possibly related to cluster aggregation into nanoparticles and/or Ag oxidation or sulfidation. The AgNC@ZnO Tp hybrids can be a potential material for sensing, anti-microbial, and photocatalysis-related applications. However, further work on improving the stability would be needed for their efficient applicability.

Author contributions

JR, NBS, MRC and TM performed Raman, steady-state PL, PLE, TRPL, density and temperature-dependent PL measurements, as well as the analysis of all the optical data. JR and TM were responsible for the revised version of the manuscript. I. C. conceived the idea, coordinated the experiments and analysed the data. CB performed the synthesis of Ag nanoclusters, composites and made morphological, structural and stability evaluations. YKM and RA synthesized ZnO tetrapods. MK performed TEM measurements. WP and LK discussed the data. All authors contributed to the discussion and writing of the manuscript.

Conflicts of interest

There are no conflicts to declare.

Acknowledgements

This work was developed within the scope of the project i3N, UIDB/50025/2020 & UIDP/50025/2020, financed by national funds through the FCT/MEC, as well as financially supported by FEDER funds through the COMPETE 2020 Programme and National Funds through FCT - Portuguese Foundation for Science and Technology under project PTDC/NAN-MAT/28755/2017 (POCI-01-0145-FEDER-028755). Funding by the Deutsche Forschungsgemeinschaft (DFG) under projects KI 1263/15-1, CRC 1261, FOR 2093, GRK 2154 is acknowledged. This work is also supported by the Cluster of Excellence "Advanced Imaging of Matter" (EXC 2056 - project ID 390715994) and GRK 2536 "Hybrid structures on the nanoscale: Chemical concepts to prepare heterogeneous nanostructures with anisotropic material properties (NANOHYBRID)" of the DFG.

References

1 I. Chakraborty and T. Pradeep, *Chem. Rev.*, 2017, **117**, 8208–8271.
2 R. Jin, C. Zeng, M. Zhou and Y. Chen, *Chem. Rev.*, 2016, **116**, 10346–10413.
3 R. Jin, *Nanoscale*, 2010, **2**, 343–362.
4 I. Chakraborty, A. Govindarajan, J. Erusappan, A. Ghosh, T. Pradeep, B. Yoon, R. L. Whetten and U. Landman, *Nano Lett.*, 2012, **12**, 5861–5866.
5 I. Chakraborty, T. Udayabhaskararao and T. Pradeep, *Chem. Commun.*, 2012, **48**, 6788.
6 I. Chakraborty, J. Erusappan, A. Govindarajan, K. S. Sugi, T. Udayabhaskararao, A. Ghosh and T. Pradeep, *Nanoscale*, 2014, **6**, 8024–8031.
7 I. Chakraborty, S. Mahata, A. Mitra, G. De and T. Pradeep, *Dalt. Trans.*, 2014, **43**, 17904–17907.
8 C. P. Joshi, M. S. Bootharaju, M. J. Alhilaly and O. M. Bakr, *J. Am. Chem. Soc.*, 2015, **137**, 11578–11581.
9 L. G. AbdulHalim, M. S. Bootharaju, Q. Tang, S. Del Gobbo, R. G. AbdulHalim, M. Eddaoudi, D. Jiang and O. M. Bakr, *J. Am. Chem. Soc.*, 2015, **137**, 11970–11975.
10 A. Desireddy, B. E. Conn, J. Guo, B. Yoon, R. N. Barnett, B. M. Monahan, K. Kirschbaum, W. P. Griffith, R. L. Whetten, U. Landman and T. P. Bigioni, *Nature*, 2013, **501**, 399–402.
11 H. Yang, Y. Wang, H. Huang, L. Gell, L. Lehtovaara, S. Malola, H. Häkkinen and N. Zheng, *Nat. Commun.*, 2013, **4**, 2422.
12 A. Som, I. Chakraborty, T. A. Maark, S. Bhat and T. Pradeep, *Adv. Mater.*, 2016, **28**, 2827–2833.
13 A. Som and T. Pradeep, *Nanoscale*, 2012, **4**, 4537.
14 A. Ghosh, T. Pradeep and J. Chakrabarti, *J. Phys. Chem. C*, 2014, **118**, 13959–13964.
15 N. Wang, Q. Sun and J. Yu, *Adv. Mater.*, 2019, **31**, 1803966.
16 D. Chen and J. Li, *Nanoscale Horizons*, 2020, **5**, 1355–1367.
17 D. Smazna, J. Rodrigues, S. Shree, V. Postica, G. Neubüser, A. F. Martins, N. Ben Sedrine, N. K. Jena, L. Siebert, F. Schütt, O. Lupan, R. Ahuja, M. R. Correia, T. Monteiro, L. Kienle, Y. Yang, R. Adelung and Y. K. Mishra, *Nanoscale*, 2018, **10**, 10050–10062.
18 J. Rodrigues, D. Smazna, N. Ben Sedrine, E. Nogales, R. Adelung, Y. K. Mishra, B. Mendez, M. R. Correia and T. Monteiro, *Nanoscale Adv.*, 2019, **1**, 1516–1526.
19 Y. K. Mishra and R. Adelung, *Mater. Today*, 2018, **21**, 631–651.
20 V. Postica, J. Gröttrup, R. Adelung, O. Lupan, A. K. Mishra, N. H. de Leeuw, N. Ababii, J. F. C. Carreira, J. Rodrigues, N. Ben Sedrine, M. R. Correia, T. Monteiro, V. Sontea and Y. K. Mishra, *Adv. Funct. Mater.*, 2017, **27**, 1604676.
21 H. Morkoç and Ü. Özgür, *Zinc Oxide: Fundamentals, Materials and Device Technology*, John Wiley & Sons, 2008.
22 U. Özgür, Y. I. Alivov, C. Liu, A. Teke, M. A. Reshchikov, S. Doğan, V. Avrutin, S.-J. Cho and H. Morkoç, *J. Appl. Phys.*, 2005, **98**, 041301.

23 J. Rodrigues, A. J. S. Fernandes, T. Monteiro and F. M. Costa, *CrystEngComm*, 2019, **21**, 1071–1090.
24 C. Klingshirn, *Phys. status solidi*, 2007, **244**, 3027–3073.
25 J. Rodrigues, N. Ben Sedrine, M. R. Correia and T. Monteiro, *Mater. Today Chem.*, 2020, **16**, 100243.
26 A. M. Abdelmonem, B. Pelaz, K. Kantner, N. C. Bigall, P. del Pino and W. J. Parak, *J. Inorg. Biochem.*, 2015, **153**, 334–338.
27 J. A. Anta, E. Guillén and R. Tena-Zaera, *J. Phys. Chem. C*, 2012, **116**, 11413–11425.
28 V. M. Markushev, V. V. Ursaki, M. V. Ryzhkov, C. M. Briskina, I. M. Tiginyanu, E. V. Rusu and A. A. Zakhidov, *Appl. Phys. B*, 2008, **93**, 231–238.
29 D. Calestani, M. Villani, M. Culiolo, D. Delmonte, N. Coppedè and A. Zappettini, *Sensors Actuators B Chem.*, 2017, **245**, 166–170.
30 D. Nunes, A. Pimentel, A. Gonçalves, S. Pereira, R. Branquinho, P. Barquinha, E. Fortunato and R. Martins, *Semicond. Sci. Technol.*, 2019, **34**, 043001.
31 E. Fortunato, A. Gonçalves, A. Pimentel, P. Barquinha, G. Gonçalves, L. Pereira, I. Ferreira and R. Martins, *Appl. Phys. A*, 2009, **96**, 197–205.
32 A. B. Djurisic, A. M. C. Ng and X. Y. Chen, *Prog. Quantum Electron.*, 2010, **34**, 191–259.
33 J. Rodrigues, A. Pimentel, E. Fortunato, T. Monteiro and F. M. Costa, *Phys. status solidi*, 2018, **215**, 1800155.
34 W.-H. Lin, Y.-H. Chiu, P.-W. Shao and Y.-J. Hsu, *ACS Appl. Mater. Interfaces*, 2016, **8**, 32754–32763.
35 N. S. Han, D. Kim, J. W. Lee, J. Kim, H. S. Shim, Y. Lee, D. Lee and J. K. Song, *ACS Appl. Mater. Interfaces*, 2016, **8**, 1067–1072.
36 M. Hoppe, O. Lupan, V. Postica, N. Wolff, V. Duppel, L. Kienle, I. Tiginyanu and R. Adelung, *Phys. Status Solidi Appl. Mater. Sci.*, 2018, **215**, 1700772.
37 O. Lupan, V. Postica, J. Gröttrup, A. K. Mishra, N. H. de Leeuw, J. F. C. Carreira, J. Rodrigues, N. Ben Sedrine, M. R. Correia, T. Monteiro, V. Cretu, I. Tiginyanu, D. Smazna, Y. K. Mishra and R. Adelung, *ACS Appl. Mater. Interfaces*, 2017, **9**, 4084–4099.
38 J. Rodrigues, M. Hoppe, N. Ben Sedrine, N. Wolff, V. Duppel, L. Kienle, R. Adelung, Y. K. Mishra, M. R. P. Correia and T. Monteiro, *Nanoscale Adv.*, , DOI:10.1039/C9NA00730J.
39 J. Rodrigues, S. Medeiros, P. M. Vilarinho, M. E. V. Costa and T. Monteiro, *Phys. Chem. Chem. Phys.*, , DOI:10.1039/D0CP00091D.
40 O. Lupan, F. Schütt, V. Postica, D. Smazna, Y. K. Mishra and R. Adelung, *Sci. Rep.*, 2017, **7**, 14715.
41 J. Rodrigues, D. Mata, A. Pimentel, D. Nunes, R. Martins, E. Fortunato, A. J. Neves, T. Monteiro and F. M. Costa, *Mater. Sci. Eng. B*, 2015, **195**, 38–44.
42 J. Rodrigues, J. Zanoni, G. Gaspar, A. J. S. Fernandes, A. F. Carvalho, N. F. Santos, T. Monteiro and F. M. Costa, *Nanoscale Adv.*, 2019, **1**, 3252–3268.
43 P. T. K. Chin, M. van der Linden, E. J. van Harten, A. Barendregt, M. T. M. Rood, A. J. Koster, F. W. B. van Leeuwen, C. de Mello Donega, A. J. R. Heck and A. Meijerink, *Nanotechnology*, 2013, **24**, 075703.
44 L. Zhu, M. Gharib, C. Becker, Y. Zeng, A. R. Ziefuß, L. Chen, A. M. Alkilany, C. Rehbock, S. Barcikowski, W. J. Parak and I. Chakraborty, *J. Chem. Educ.*, 2020, **97**, 239–243.
45 Y. K. Mishra, S. Kaps, A. Schuchardt, I. Paulowicz, X. Jin, D. Gedamu, S. Freitag, M. Claus, S. Wille, A. Kovalev, S. N. Gorb and R. Adelung, *Part. Part. Syst. Charact.*, 2013, **30**, 775–783.
46 I. Paulowicz, V. Postica, O. Lupan, N. Wolff, S. Shree, A. Cojocaru, M. Deng, Y. K. Mishra, I. Tiginyanu, L. Kienle and R. Adelung, *Sensors Actuators B Chem.*, 2018, **262**, 425–435.
47 R. Cuscó, E. Alarcón-Lladó, J. Ibáñez, L. Artús, J. Jiménez, B. Wang and M. Callahan, *Phys. Rev. B*, 2007, **75**, 165202.
48 J. Serrano, F. J. Manjón, A. H. Romero, A. Ivanov, M. Cardona, R. Lauck, A. Bosak and M. Krisch, *Phys. Rev. B*, 2010, **81**, 174304.
49 F. J. Manjón, B. Marí, J. Serrano and A. H. Romero, *J. Appl. Phys.*, 2005, **97**, 053516.
50 R. P. Wang, G. Xu and P. Jin, *Phys. Rev. B*, 2004, **69**, 113303.
51 J. Rodrigues, A. J. S. Fernandes, D. Mata, T. Holz, R. G. Carvalho, R. Fath Allah, T. Ben, D. Gonzalez, R. F. Silva, A. F. da Cunha, M. R. Correia, L. C. Alves, K. Lorenz, A. J. Neves, F. M. Costa and T. Monteiro, in *SPIE OPTO*, eds. F. H. Teherani, D. C. Look and D. J. Rogers, International Society for Optics and Photonics, 2014, p. 89871F.
52 L. Bergman, X.-B. Chen, J. Huso, J. L. Morrison and H. Hoeck, *J. Appl. Phys.*, 2005, **98**, 093507.
53 T. Sander, S. Eisermann, B. K. Meyer and P. J. Klar, *Phys. Rev. B*, 2012, **85**, 165208.
54 M. A. Moyano, A. M. Broussalis and A. I. Segall, *J. Therm. Anal. Calorim.*, 2010, **99**, 631–637.
55 N. Ikuta, A. Tanaka, A. Otsubo, N. Ogawa, H. Yamamoto, T. Mizukami, S. Arai, M. Okuno, K. Terao and S. Matsugo, *Int. J. Mol. Sci.*, 2014, **15**, 20469–20485.
56 A. Tereshchenko, M. Bechelany, R. Viter, V. Khranovskyy, V. Smyntyna, N. Starodub and R. Yakimova, *Sensors Actuators, B Chem.*, 2016, 229, 664–677.
57 B. Adhikari and A. Banerjee, *Chem. Mater.*, 2010, **22**, 4364–4371.
58 H. Xu and K. S. Suslick, *Adv. Mater.*, 2010, **22**, 1078–1082.
59 I. Díez and R. H. A. Ras, *Nanoscale*, 2011, **3**, 1963.
60 X. Yuan, M. I. Setyawati, A. S. Tan, C. N. Ong, D. T. Leong and J. Xie, *NPG Asia Mater.*, 2013, **5**, e39.
61 T. Monteiro, A. J. Neves, M. C. Carmo, M. J. Soares, M. Peres, J. Wang, E. Alves, E. Rita and U. Wahl, *J. Appl. Phys.*, 2005, **98**, 013502.
62 I. Díez and R. H. A. Ras, Springer, Berlin, Heidelberg, 2010, pp. 307–332.
63 J. P. Wilcoxon, J. E. Martin and P. Provencio, *J. Chem. Phys.*, 2001, **115**, 998–1008.
64 C. Jagadish and S. Pearton, *Zinc Oxide Bulk, Thin Films and Nanostructures*, Elsevier, 2006.
65 A. B. Djurišić, Y. H. Leung, K. H. Tam, Y. F. Hsu, L. Ding, W. K. Ge, Y. C. Zhong, K. S. Wong, W. K. Chan, H. L. Tam, K. W. Cheah, W. M. Kwok and D. L. Phillips, *Nanotechnology*, 2007, **18**, 095702.

66 T. Schmidt, K. Lischka and W. Zulehner, *Phys. Rev. B*, 1992, **45**, 8989–8994.

67 K. Tanaka, Y. Miyamoto, H. Uchiki, K. Nakazawa and H. Araki, *Phys. status solidi*, 2006, **203**, 2891–2896.

68 P. Y. Yu and M. Cardona, *Fundamentals of Semiconductors*, Springer Berlin Heidelberg, Berlin, Heidelberg, 2005.

69 A. B. Djurišić, Y. H. Leung, K. H. Tam, L. Ding, W. K. Ge, H. Y. Chen and S. Gwo, *Appl. Phys. Lett.*, 2006, **88**, 103107.

70 M. A. Reshchikov, H. Morkoç, B. Nemeth, J. Nause, J. Xie, B. Hertog and A. Osinsky, *Phys. B Condens. Matter*, 2007, **401**–**402**, 358–361.

71 A. F. Kohan, G. Ceder, D. Morgan and C. G. Van De Walle, *Phys. Rev. B*, 2000, **61**, 19–27.

72 R. Dingle, *Phys. Rev. Lett.*, 1969, **23**, 579–581.

73 S. L. Shi, G. Q. Li, S. J. Xu, Y. Zhao and G. H. Chen, *J. Phys. Chem. B*, 2006, **110**, 10475–10478.

74 J. Fallert, R. Hauschild, F. Stelzl, A. Urban, M. Wissinger, H. Zhou, C. Klingshirn and H. Kalt, *J. Appl. Phys.*, 2007, **101**, 073506.

75 S. S. Kurbanov and T. W. Kang, *J. Lumin.*, 2010, **130**, 767–770.

76 M. Schirra, R. Schneider, A. Reiser, G. M. Prinz, M. Feneberg, J. Biskupek, U. Kaiser, C. E. Krill, K. Thonke and R. Sauer, *Phys. Rev. B*, 2008, **77**, 125215.

77 D. Tainoff, B. Masenelli, P. Melinon, A. Belsky, G. Ledoux, D. Amans, C. Dujardin, N. Fedorov and P. Martin, *J. Lumin.*, 2009, **129**, 1798–1801.

78 K. Thonke, M. Schirra, R. Schneider, A. Reiser, G. M. Prinz, M. Feneberg, J. Biskupek, U. Kaiser and R. Sauer, *Microelectronics J.*, 2009, **40**, 210–214.

79 D. Tainoff, B. Masenelli, P. Mélinon, A. Belsky, G. Ledoux, D. Amans, C. Dujardin, N. Fedorov and P. Martin, *Phys. Rev. B*, 2010, **81**, 115304.

80 J. Rodrigues, T. Holz, R. Fath Allah, D. Gonzalez, T. Ben, M. R. Correira, T. Monteiro and F. M. Costa, *Sci. Rep.*, 2015, **5**, 10783.

81 I. Unlu, J. W. Soares, D. M. Steeves and J. E. Whitten, *Langmuir*, 2015, **31**, 8718–8725.

82 J. Im, J. Singh, J. W. Soares, D. M. Steeves and J. E. Whitten, *J. Phys. Chem. C*, 2011, **115**, 10518–10523.

83 P. W. Sadik, S. J. Pearton, D. P. Norton, E. Lambers and F. Ren, *J. Appl. Phys.*, 2007, **101**, 104514.